ACS OMEGA

Open Access

http://pubs.acs.org/journal/acsodf

Article

Analysis of Flow Field Characteristics in a Mechanical Defoaming Device

Shuai Li, Tiefeng Peng, Shaomei Xu, Youjie Qiu, and Yangyang Huai*

Cite This: *ACS Omega* 2024, 9, 42850−42857

Read Online

ACCESS | Metrics & More | Article Recommendations

ABSTRACT: To improve the froth breakdown performance of flotation foam, a mechanical defoaming device based on vacuum and rotation was developed. The device is mainly composed of a rotating disk and a baffle and generates negative pressure when rotating at high speed. Through the synergistic effects of negative pressure, collision, extrusion, and shearing, the flotation foam effectively separates the liquid and gas phases. The flow field characteristics of the defoaming device are meticulously analyzed through numerical simulation, leading to a comprehensive evaluation of its defoaming performance. The effects of different rotational speeds on fluid velocity, pressure, turbulence, and traces are studied. It can be obtained that when the rotational speed is 900−1800 rpm, the device generates a pressure zone of −2.5 to −12.5 kPa, which can meet the requirements of the defoaming design.

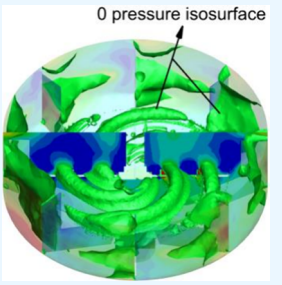

1. INTRODUCTION

Bubbles and foams are frequently encountered in the daily lives and professional environments of individuals. Through the application of soaps and surfactants, one is able to visually perceive and tactilely experience the formation and subsequent rupture of bubbles.[1] The volumetric gravity of a foam body is influenced by the ratio of the mass of liquid contained in the foam to the mass of gas, which is related to the difference in the thickness of the intermediate liquid film.[1] Owing to its membranous structure, foam represents a thermodynamically unstable two-phase system that undergoes intricate processes such as gravity drainage, agglomeration, and Ostwald maturation.[2−4]

During the process of foam formation, the liquid transforms into a thin film of bubbles, giving rise to polyhedral irregular bubbles.[1] The consensus among most scholars is that the foam itself represents a thermodynamically unstable system, but highly stable foam systems are formed when they interact with surfactants (e.g., most cationic surfactants). Foam stability is affected by a variety of factors, including surface tension, elasticity of the foam film, viscosity of the liquid, bubble size and distribution, temperature, pressure, additives, nature of the gas, external disturbances, etc.[5−7]

In chemical production, it is often necessary to separate and extract different phases, such as separating gas or solid particles from liquids or extracting and separating two or more different liquid phases from another. Flotation is a sophisticated separation process predicated on the differential wettability exhibited by solid particles.[1] Based on the distinct surface properties of various mineral particles, foam is utilized to separate the minerals in the flotation feed from gangue minerals, thus enriching the target minerals.[1,8,9] Hence, the formation, characteristics, and endurance of the foam play pivotal roles in the flotation process. However, the robust stability of this foam poses a significant obstacle to the subsequent processing of the recovered concentrate within it.[1]

Presently, there exist two primary methods for defoaming: chemical defoaming and physical defoaming.[1] The chemical defoaming method reduces surface tension and viscosity to rupture foam, whereas the physical defoaming method disrupts the liquid film with external forces to achieve the same result.[1] Huang et al.[10] conducted an evaluation of the efficacy of a silicone oil defoamer (G) and an emulsified hydrocarbon oil defoamer (R) in mitigating foam formation during the flotation process for clean coal. They investigated the effect of the addition method and amount of defoamer on the defoaming effect of flotation clean coal as well as the impact of the remaining defoamer in the circulating water on the flotation process. The results indicate that an increase in the amount of defoamer leads to a better defoaming effect, with silicone oil defoamer outperforming the emulsified hydrocarbon oil defoamer. The residue of a lower amount of defoamer in the circulating water has a minimal impact on flotation. However, when there is a large residual amount, the silicone oil defoamer reduces flotation selectivity and inhibits the process. Bhakta et al.[11] discussed the relationship between surface tension and froth stability and how froth stability can be controlled by adjusting the concentration of surfactant. Wu et al.[12] found that the static defoaming method cannot

Received: May 29, 2024
Revised: September 14, 2024
Accepted: September 17, 2024
Published: October 9, 2024

effectively eliminate the three-phase foam. The warming method can quickly and effectively eliminate the three-phase foam, but the energy consumption is high; the mechanical stirring defoaming can eliminate a large number of foams, but it is easy to generate secondary froth problems in the conveying process; the water spraying defoaming method has better defoaming effect, but it consumes a large amount of water. The research results of Liqin et al.[13] show that low vacuum and short defoaming time can achieve a better defoaming effect, which is easy to realize in the industry and has the prospect of production application.

Takesono et al.[14] conducted a study on the foam breakdown characteristics of a mechanical foam-breaker using shear force (MFUS) in a stirred-tank reactor (STR), where a fixed orifice plate and a rotating disk were utilized. The study revealed the effects of operating conditions on the liquid holdup in foam and the volumetric rate of foam flow, which are indicative of the foaming behavior of the STR. The following study[15] details the experimentation of a novel foam breaker, which operates on the principle of shearing action induced by a high-speed rotating disk. The results indicate that within the parameters investigated, foam located 3 cm from the center of rotation of the disk collapsed entirely at speeds of approximately 2500 rpm, irrespective of foam flow rate and material composition. Wang[16] has proposed a novel form of mechanical foam disruptor that operates on the principle of self-oscillation. Through simulation, it has been demonstrated that the combined influence of negative pressure, collision, extrusion, and shear within the cavity results in the fracturing of the foam. Liu et al.[17] innovatively developed a cutting-edge froth defoamer equipped with perforated plates to augment the defoaming process. The findings demonstrated that the utilization of perforated plates could significantly bolster bubble coalescence or bubble collapse, thereby enhancing the overall defoaming efficiency. Garrett[18] provided a comprehensive exposition on the theory and methodology of defoaming utilizing a rotary apparatus in conjunction with ultrasonic waves. To eliminate foam, physical methods that can be used include mechanical stirring, heating, radiation irradiation, and high-frequency vibration. Under the action of the physical method, the decay rate of the foam will be greatly increased, which helps to reduce the number of foams.[18,19]

A new defoaming device is designed by combining mechanical and vacuum defoaming methods in this study.[1] Through real computational fluid dynamics (CFD) simulation, the flow field characteristics of the defoaming device can be analyzed in detail, providing a foundation for enhancing the device's design and operation. Understanding the flow field characteristics helps to improve the defoaming efficiency, reduce energy consumption, and ensure effective foam control in industrial processes.

2. MATHEMATICAL MODELS

2.1. Flow Control Equations. The flow control equations describe the conservation of momentum, mass, and energy of fluid in the flow process. In fluid mechanics, the flow control equations usually include continuity equations, momentum equations, and energy equations.

The continuity equation delineates the conservation of mass for the fluid; i.e., the mass flow through a section per unit time is equal to the reduction rate of the mass flowing through the section. It can be articulated in the subsequent format:

$$\partial_\rho/\partial_t + \nabla\cdot(\rho\vec{u}) = 0 \tag{1}$$

where ρ is the fluid density, $\vec{u}$ is the flow velocity vector, and t is the time.

The momentum equation describes the conservation of momentum of the fluid; i.e., the momentum flow through a section per unit time is equal to the reduction rate of momentum through the section. It can be expressed in the following form:

$$\partial(\rho\vec{u})/\partial_t + \nabla\cdot(\rho\vec{u}\vec{u}) = -\nabla P + \mu\nabla\text{^}2\vec{u} + \rho g \tag{2}$$

where ρ is the fluid density, $\vec{u}$ is the flow velocity vector, P is the pressure, μ is the dynamic viscosity, and g is the acceleration of gravity.

The energy equation describes the conservation of fluid energy; i.e., the energy flow through a section per unit time is equal to the reduction rate of energy flowing through the section. It can be expressed as follows:

$$\partial(\rho E)/\partial_t + \nabla\cdot(\rho E\vec{u}) = -\nabla\cdot(P\vec{u}) + \nabla\cdot(k\nabla T) + \rho g\vec{u} \tag{3}$$

where E is the total energy per unit mass, T is the temperature of the fluid, k is the thermal conductivity, ρ is the density of the fluid, t is the time, $\vec{u}$ is the velocity vector, P is the pressure, and g is the acceleration of gravity.

2.2. Turbulence Model. Turbulence occurs in regions where there is a change in speed, resulting in a nonlinear and complex flow. The Lagrange method and Euler method are the two most commonly used approaches for analyzing multiphase flows. In Euler's method, each phase can be described by a set of conservation equations.[20−22] The closure of the equations is achieved through the application of constitutive relations or statistical kinematics theory. Euler methods encompass a range of sophisticated models, including volume of fluid (VOF) models, mixture models, and Euler models. In this study, the Eulerian model is adopted because it is suitable for dealing with large-scale two-phase flow problems, such as the movement of bubbles in liquids and the dissolution of gases in liquids.

The continuity equation of the qth phase in the Euler model can be expressed as[22]

$$\frac{\partial}{\partial t}(\alpha_q\rho_q) + \nabla\cdot(\alpha_q\rho_q\vec{v_q}) = \sum_{p=1}^{n}(\dot{m}_{qp} - \dot{m}_{pq}) + S_q \tag{4}$$

where $\vec{v_q}$, $\dot{m}_{qp}$, and $\dot{m}_{pq}$ represent the velocity of the qth phase, the mass transfer from phase q to phase p, and the mass transfer from phase p to phase q, respectively. S_q is the source item, initially set to a default value of 0.[22]

The momentum equation of the qth phase in the Euler model can be expressed as[22]

$$\begin{aligned}\frac{\partial}{\partial t}(\alpha_q\rho_q\vec{v_q}) + \nabla\cdot(\alpha_q\rho_q\vec{v_q}\vec{v_q}) &= -\alpha_q\nabla p + \nabla\cdot\bar{\bar{\tau}}_q + \alpha_q\rho_q\vec{g} + \sum_{p=1}^{n}(\vec{R}_{pq} + \dot{m}_{pq}\vec{v}_{pq} \\ &\quad - \dot{m}_{qp}\vec{v}_{qp}) + (\vec{F_q} + \vec{F}_{\text{lift},q} + \vec{F}_{vm,q})\end{aligned} \tag{5}$$

where $\vec{g}$ is the acceleration of gravity and $\bar{\bar{\tau}}_q$ is the stress−strain tensor of the qth phase:

$$\bar{\bar{\tau}}_q = \alpha_q\mu_q(\nabla\vec{v_q} + \nabla\vec{v_q}^T) + \alpha_q(\lambda_q - \frac{2}{3}\mu_q)\nabla\cdot\vec{v_q}\bar{\bar{I}} \tag{6}$$

https://doi.org/10.1021/acsomega.4c04351
ACS Omega 2024, 9, 42850−42857

where μ_q, λ_q, $\vec{F}_q$, $\vec{F}_{\text{lift},q}$, $\vec{F}_{vm,q}$ and $\vec{R}_{pq}$represent the shear viscosity coefficient, volume viscosity coefficient, external volume force, lift force, virtual mass force, and interphase interaction force, respectively.[22]

The transport equations for k and ε in the realizable $k-\varepsilon$ turbulence model are[22]

$$\frac{\partial(\rho k)}{\partial t} + \frac{\partial(\rho k u_i)}{\partial x_i} = \frac{\partial}{\partial x_j}[(\mu + \frac{\mu_t}{\partial_k})\frac{\partial k}{\partial x_j}] + G_k - \rho\varepsilon \tag{7}$$

$$\frac{\partial(\rho\varepsilon)}{\partial t} + \frac{\partial(\rho\varepsilon u_i)}{\partial x_i} = \frac{\partial}{\partial x_j}[(\mu + \frac{\mu_t}{\partial_\varepsilon})\frac{\partial \varepsilon}{\partial x_j}] + \rho C_1 E\varepsilon - \rho C_2 \frac{\varepsilon^2}{k + \sqrt{\nu\varepsilon}} \tag{8}$$

where$\mu_t = \rho C_\mu \frac{k^2}{\varepsilon}$, $C_\mu = \frac{1}{A_0 + A_S U^{*k}/_\varepsilon}$, and U^* are used to indicate the effect of rotation.

2.3. Foam Rheology Modeling. The mathematical modeling of foam rheology presents a significant challenge, primarily due to the limited understanding of its microstructure and the inherent instabilities caused by gravity drainage and bubble aggregation processes.[23] Most theoretical models for foam viscosity treat foams as Newtonian and incompressible fluids, limiting them to low-mass aqueous foams. Foam viscosity is typically expressed as a function of base fluid viscosity, foam mass, and the dimensionless capillary number Ca, which measures bubble deformation in a steady foam flow. For Newton-based fluids, the capillary number is described as[3]

$$C_a = \frac{\gamma_b \dot{\gamma} \eta_L}{\sigma} \tag{9}$$

where γ_b = average bubble radius, $\dot{\gamma}$ = shear rate, η_L = liquid viscosity, and σ = interfacial tension (surface tension). When $C \ll 1$, interfacial forces prevail and spherical bubbles are formed, leading to maximum distortion of the flow line, which results in an increase in the viscosity of the suspension.[24] However, when $C_a \gg 1$, viscous forces dominate, and the bubbles elongate along the flow direction, resulting in less streamline distortion, a larger free slip area, and therefore a decrease in suspension viscosity.[25]

2.4. Model Grid. A mechanical defoaming device with a diameter of 1000 mm and a height of 600 mm is designed for simulation. Its main structure includes a rotating disc and a baffle, as shown in Figure 1. The device is divided into 3D units using the unstructured grid method, with two common methods for dealing with rotating regions in rotating machinery being the multireference system and sliding grid methods.

The multiple reference frame method is an approximate calculation technique for analyzing steady flow fields utilizing two reference frames.[26−28] The rotating coordinate system is utilized as the reference system within the moving region of the agitator blade, whereas the static coordinate system is employed in the remaining regions.[22,29] The sliding grid method is capable of addressing unsteady problems,[30,31] which sets it apart from the MRF model. In a sliding grid system, the relative movement between the stationary and rotating components induces a transient interaction effect, leading to the transformation and transmission of generated data through the interface.[22] This represents the key distinction between the two models.

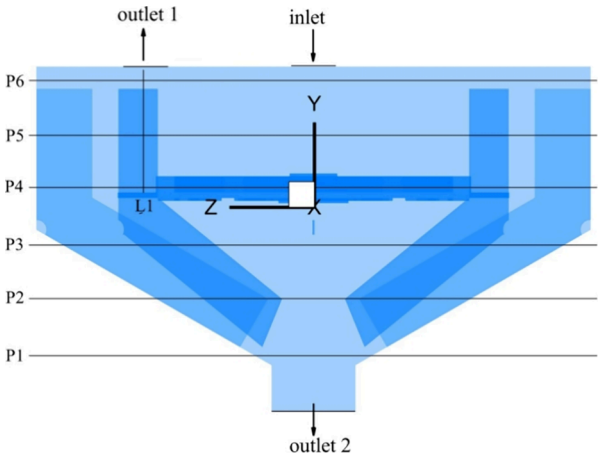

Figure 1. Structural diagram of the mechanical defoaming device.

In this study, a sliding mesh is used:[32]

$$\frac{d}{dt}\int_V \rho\varphi dV + \int_{\partial V} \rho\varphi((\vec{u} - \vec{u_g}))\cdot dA = \int_{\partial V} \Gamma\nabla\varphi\cdot dA + \int_V S_\varphi dV \tag{10}$$

where ρ is the fluid density, $\vec{u}$ is the flow velocity vector, $\vec{u_g}$ is the mesh velocity of the moving mesh, Γ is the diffusion coefficient, and S_φ is the source term. V refers to the boundary of control volume.[32]

In the context of the sliding grid, the derivative with respect to time can be expressed as follows:[32]

$$\frac{d}{dt}\int_V \rho\varphi dV = \frac{[(\rho\varphi)^{n+1} - (\rho\varphi)^n]V}{\Delta t} \tag{11}$$

where n and $n + 1$ represent the present moment as well as the subsequent moment.

3. SIMULATION SETUP

In view of the strong negative pressure, collision, shear, and other effects generated by the defoamer during operation, FLUENT is selected to calculate the flow field characteristics. In the Euler−Euler method employed by FLUENT, different phases are conceptually treated as a continuous entity interpenetrating with one another. The spatial occupation of one phase precludes that of other phases, and the volume fraction of all phases is posited to be a continuous spatiotemporal function, with their collective sum equating to unity.

The working conditions in FLUENT were defined by the following parameters: the gas−liquid mixture entered with an inlet velocity of 0.189 m/s, whereas the viscosity of the liquid was measured at 0.0003 kg·m^{-1}·s^{-1}. The model employed a velocity inlet boundary at the entrance and a pressure outlet boundary at the exit.[32] Spatial discretization utilized a first-order upwind scheme, and the coupling of velocity and pressure was resolved using the SIMPLE algorithm.[32] A default turbulence intensity of 5% was set for both air and slurry at their respective entrances, with their actual diameters considered as hydraulic diameter.[33]

https://doi.org/10.1021/acsomega.4c04351
ACS Omega 2024, 9, 42850−42857

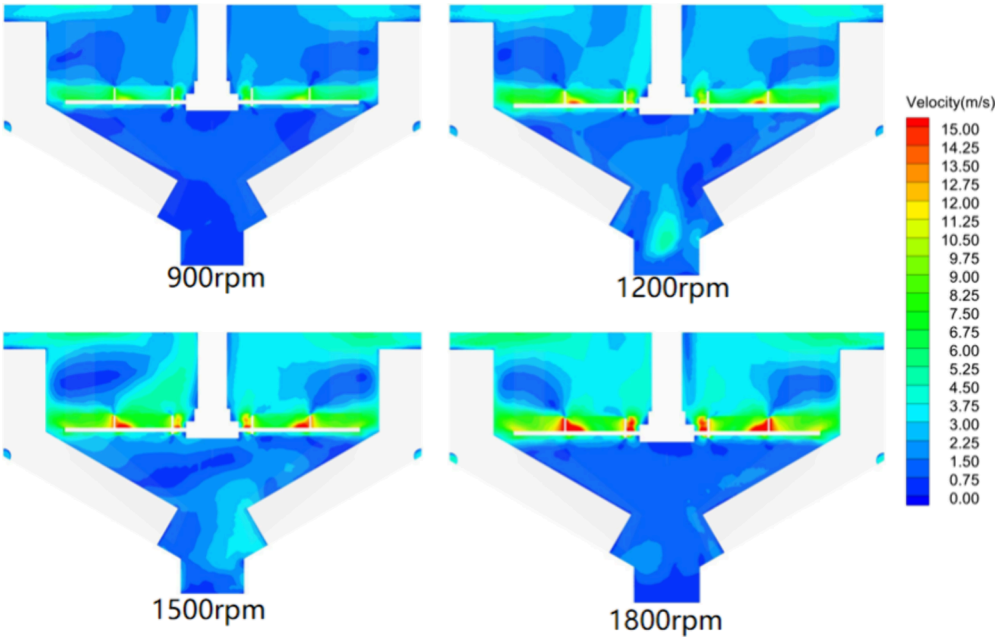

Figure 2. Velocity contour on the $X = 0$ surface at different rotational speeds.

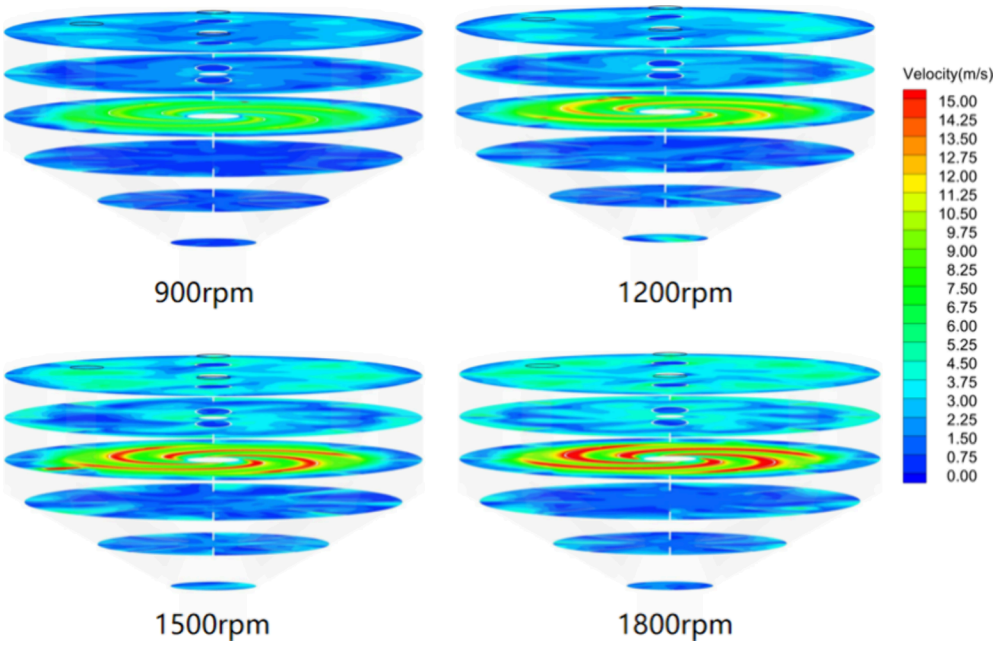

Figure 3. Velocity contour on P1−P6 surfaces at different rotational speeds.

4. RESULTS AND DISCUSSIONS

As illustrated in Figure 1, the coordinate axes have been established to study the flow field using cloud images or data on six cutting surfaces (P1−P6) and a straight line (L1). This primarily involves analyzing the velocity distribution, turbulence degree, and pressure of the fluid.

4.1. Fluid Velocity Field. The rotational speed significantly influences the flow pattern and distribution of the liquid flow field. At lower rotational speeds, the liquid flow tends to be relatively smooth with a large low-speed or eddy current zone around the agitator. As the rotation speed increases, the liquid flow becomes more intense, leading to a gradual decrease in the low-speed zone around the agitator and a more uniform distribution of the flow field. For materials with high viscosity, it is advisable to increase the initial flow rate of the stirring medium appropriately. Conversely, for materials with low viscosity, reducing the initial flow rate of the stirring medium is recommended to prevent the material from splashing out.

Figure 2 shows the velocity cloud on the $X = 0$ plane. It can be evident that the velocity of the fluid is distributed in different layers, with the largest velocity near the dispersion plate and the smallest velocity at the exit. Above the dispersion plate, the fluid velocity gradually increases as the speed increases, but when the speed is ≥1500 rpm, the fluid velocity does not change much. Below the dispersion plate, the fluid velocity first increases and then decreases as the speed increases.

https://doi.org/10.1021/acsomega.4c04351
ACS Omega 2024, 9, 42850−42857

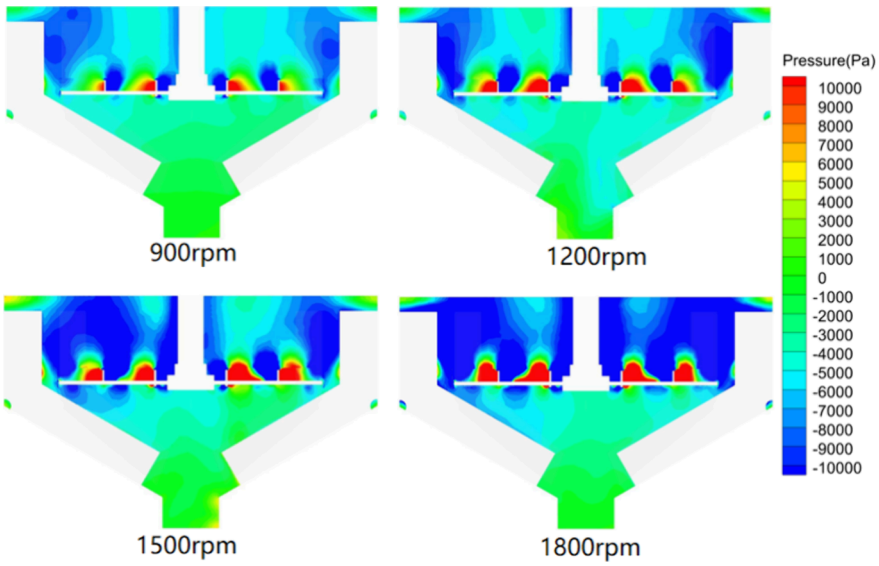

Figure 4. Pressure contour on the $X = 0$ surface at different rotational speeds.

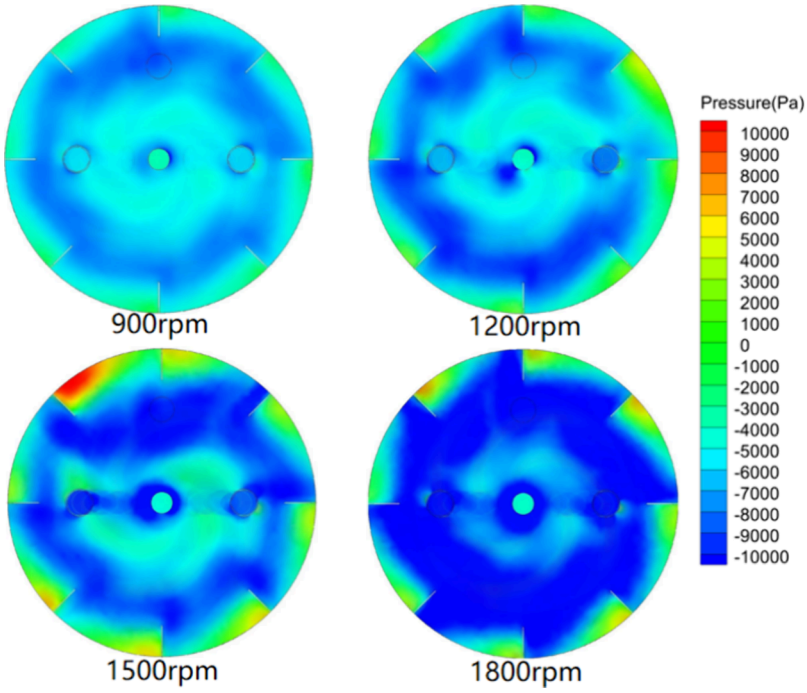

Figure 5. Volume rendering graph of pressure at different rotational speeds.

Figure 3 illustrates the velocity distribution across various sections of the Y axis. The fluid velocity undergoes significant changes in the vicinity of the baffle, indicating a collision between the fluid and the baffle. This collision phenomenon is predominantly observed within a region of similar height to that of the rotating disc.

As the rotational speed increases, the average flow rate of the liquid also increases. This indicates that the kinetic energy within the liquid is higher, and the flow becomes more active. The highest flow rate is typically near the impeller, while it decreases in areas farther from the impeller. An increase in the agitation speed enhances the shear action of the blade on the fluid, consequently increasing its shear rate. A higher shear rate generally leads to smaller and more uniform bubbles in the foam. This is due to elevated shear forces promoting bubble bursting and merging, thereby altering the foam's structure.

4.2. Pressure Distribution. The increase in the rotational speed will result in an increase in the fluid velocity, leading to a greater pressure gradient within the fluid. These pressure gradients act as driving forces for fluid flow. Pressure can impact the interactions between gas and liquid within the foam, including the gas solubility in the liquid, surface tension, and mechanical strength of the foam film.

Figure 4 illustrates the pressure distribution in the $X = 0$ section. It is evident that as the velocity increases, the static pressure above the dispersion plate gradually decreases, particularly when the speed exceeds 1500 rpm, leading to a significant expansion of the negative pressure area. The static

https://doi.org/10.1021/acsomega.4c04351
ACS Omega 2024, 9, 42850−42857

pressure below the dispersion plate remains relatively stable, although there is also a certain extent of negative pressure.

Figure 5 presents an overhead view of the static pressure volume rendering graph. The findings indicate that as the speed escalates, the volume of the negative pressure region progressively expands, reaching its peak at 1800 rpm.

When rotating at high speed, the upper part of the dispersion disk creates a negative pressure area to attract foam, as illustrated in Figure 6. The main pressure range is

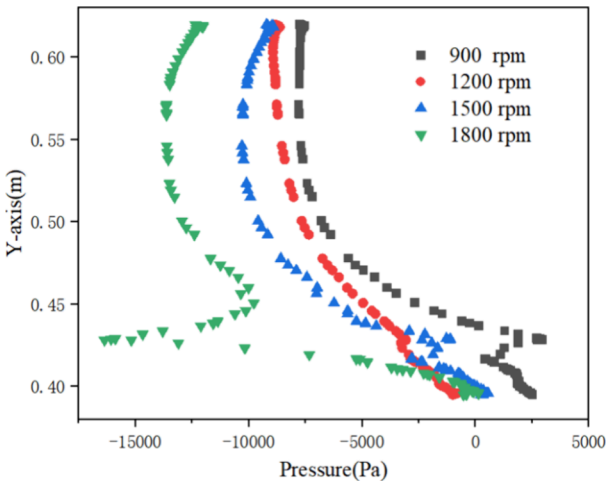

Figure 6. Static pressure values in line L1.

−2.5 to −12.5 kPa. The experimental results of Jiang[1] show that the elimination of 20 cm high flotation foam requires only one-third of the time under normal pressure at the pressure of −1 kPa. Therefore, the design of the defoaming device can meet the requirements.

By reducing the system pressure, the saturation pressure of gas in the bubble decreases, causing the bubble to release gas and shrink or disappear. Under higher negative pressure conditions, more foam can be eliminated, but this necessitates a higher impeller speed and increased energy consumption. Hence, to achieve better defoaming results while also considering energy efficiency, defoaming should be conducted under specific negative pressure conditions. Overall, a rotating disc speed of 1200−1500 rpm may be appropriate.

4.3. Gas-Phase Distribution. Increasing the rotational speed typically results in a reduction in bubble size, as higher shear forces break up larger bubbles, leading to the formation of more and smaller bubbles.

Figure 7 illustrates the gas volume fraction cloud in the X = 0 section. It is evident that the gas volume fraction gradually decreases with an increase in rotational speed, with a noticeable declining trend observed when the rotational speed exceeds 1500 rpm.

The escalation of the rotation speed can enhance the generation rate of bubbles, facilitating greater release of gas from the liquid and consequently reducing the residence time of bubbles within the liquid.

4.4. Vortex Distribution. From an energy perspective, Q represents the energy of the vortex per unit mass and per unit of space. The quantity, structure, and energy of the vortex reflect the characteristics of the external mechanical energy input to the equipment, to a certain extent. The high-speed rotation of the vortex can generate localized high shear forces

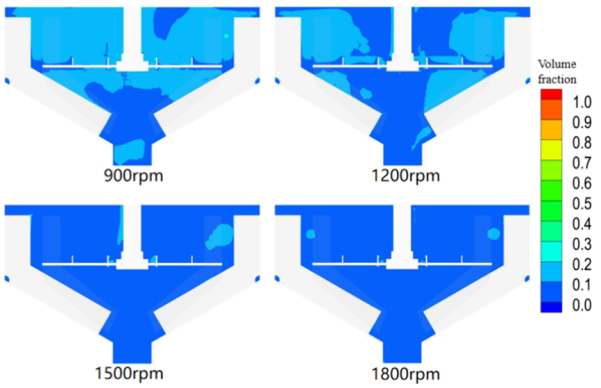

Figure 7. Gas volume fraction cloud on the X = 0 section at different rotational speeds

in the foam, which can cause the bubbles in the foam to burst, reducing the volume of the foam and altering its structure.

Figure 8 shows that the vortex mainly occurs around the baffle above the dispersion plate. With an increase in rotational speed, there is initially an increase in both the number and intensity of vortices followed by a decrease. At a rotational speed of 1800 rpm, there is a decrease in both number and intensity of vortices due to the small gas holdup at this time. The strong action of vortices may destabilize foams, especially those formed in highly viscous liquids.

4.5. Streamlines. By observing the shape, direction, and evolution of the trace, we can gain insights into the motion trajectory, velocity distribution, and potential vortex and reflux phenomena of the fluid in the flow field.

As depicted in Figure 9, upon entering the device, most fluids initially travel along the rotating disk until they reach its periphery. Under the influence of centrifugal force, they are propelled toward the surrounding baffle or vessel wall where collisions occur, or they enter a vortex around the flow for a certain period. Upon separation of gas and liquid phases, gas is discharged from the upper outlet, while liquid exits from the lower outlet.

Upon careful observation and analysis of the streamline shape, direction, and evolution, no significant vortex or reflux phenomena were observed. This indicates that there are no major issues with the fluid flow.

5. CONCLUSIONS

The flow field characteristics of the mechanical defoamer were analyzed using an air−water two-phase flow model, which included the magnitude and distribution of pressure, velocity, and turbulent intensity. This analysis has validated the operational principle and viability of the defoamer, demonstrating its effectiveness in practical application. It was determined that compression, shear, and tensile forces can be utilized to make the foam burst. Hence, the functionality of the mechanical defoaming device may be predicated upon one or more of the ensuing four mechanisms: abrupt fluctuations in pressure, application of shear force, exertion of compressive force, and impartation of the impact force.

Simulation results indicated that when the rotating speed is between 900 and 1800 rpm, the defoaming device can generate a negative pressure area ranging from −2.5 to −12.5 kPa. This suggests that the defoaming efficiency can be effectively improved. Considering energy consumption concerns, it is recommended that a speed of 1200−1500 rpm is suitable.

https://doi.org/10.1021/acsomega.4c04351
ACS Omega 2024, 9, 42850−42857

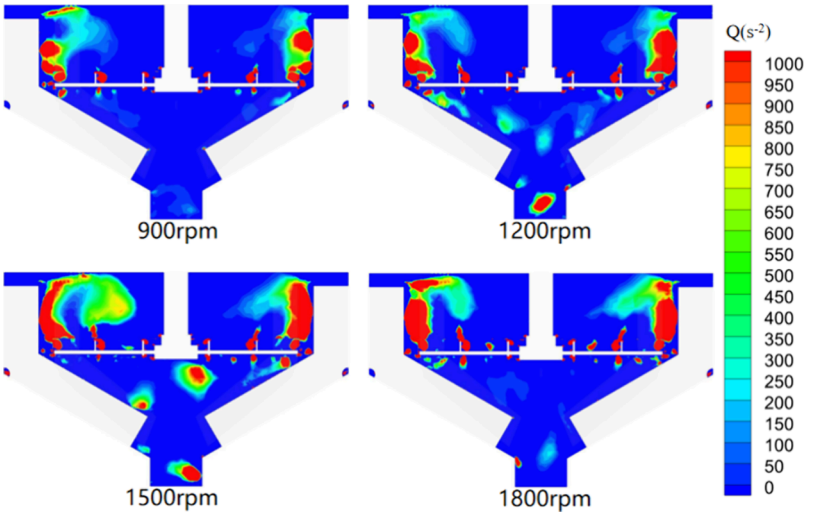

Figure 8. Cloud diagram of vortex structure distribution on the $X = 0$ section at different rotational speeds.

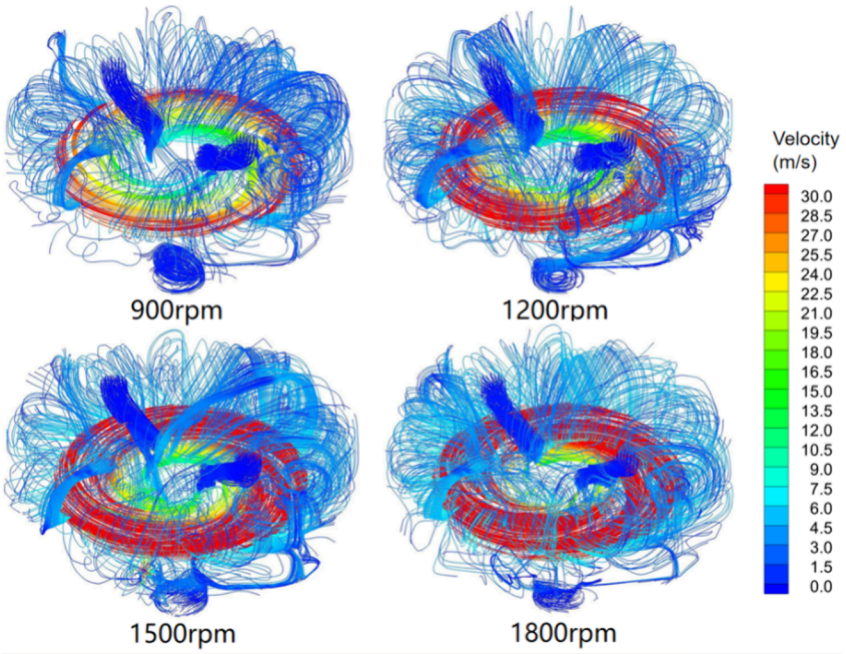

Figure 9. Fluid streamlines at different rotational speeds.

However, further investigation is necessary to develop a mathematical model for the stability of single bubbles, foam stability, and gas−liquid mass transfer in numerical simulations. These challenges are poised to become our next focal point in this area of research.

AUTHOR INFORMATION

Corresponding Author

Yangyang Huai − *Jiangxi Copper Technology Research Institute Co., Ltd., Nanchang, Jiangxi 330096, China*; Email: huai@jxcc.com

Authors

Shuai Li − *Jiangxi Copper Technology Research Institute Co., Ltd., Nanchang, Jiangxi 330096, China*; orcid.org/0000-0001-5784-0949

Tiefeng Peng − *Jiangxi Copper Technology Research Institute Co., Ltd., Nanchang, Jiangxi 330096, China*

Shaomei Xu − *Jiangxi Copper Technology Research Institute Co., Ltd., Nanchang, Jiangxi 330096, China*; orcid.org/0009-0004-3610-9566

Youjie Qiu − *Jiangxi Copper Technology Research Institute Co., Ltd., Nanchang, Jiangxi 330096, China*

Complete contact information is available at: https://pubs.acs.org/10.1021/acsomega.4c04351

Notes

The authors declare no competing financial interest.

ACKNOWLEDGMENTS

The financial support of Jiangxi Province's major science and technology research and development special project (20232ACE01010) & Jiangxi Province Double Thousand Plan (S2021LQCQ0128) is gratefully acknowledged.

REFERENCES

(1) Jiang, H.; et al. Study on Combined Vacuum−Mechanical Defoaming Technology for Flotation Froth and Its Mechanism. *Processes* **2022**, *10*, 1183.

(2) Firoze Akhtar, T.; et al. Rheological behavior of aqueous foams at high pressure. *J. Pet. Sci. Eng.* **2018**, *162*, 214−224.

(3) Sinha, V.; et al. Rheology and hydraulics of polymer-based foams at elevated temperatures. *J. Pet. Sci. Eng.* **2019**, *180*, 330−346.

(4) Obisesan, O.; Ahmed, R.; Amani, M. The Effect of Salt on Stability of Aqueous Foams. *Energies* **2021**, *14*, 279.

(5) Vinet, L.; Zhedanov, A. A 'missing' family of classical orthogonal polynomials. *Journal of Physics A: Mathematical and Theoretical* **2011**, *44* (8), No. 085201.

(6) Guo, B.; Sun, K.; Ghalambor, A. A Closed Form Hydraulics Equation for Predicting Bottom-Hole Pressure in UBD with Foam. In *SPE/IADC Managed Pressure Drilling and Underbalanced Operations Conference and Exhibition?*; SPE: 2003.

(7) Oratis, A. T.; et al. A new wrinkle on liquid sheets: Turning the mechanism of viscous bubble collapse upside down. *Science* **2020**, *369* (6504), 685−688.

(8) Taner, H. A.; Onen, V. Mechanism of Mechanical Entrainment in Chalcopyrite Flotation: Effects of Clay Minerals. *Min., Metall., Explor.* **2023**, *41* (1), 311−319.

(9) Lee, R. L. J.; Peng, Y. Assessing the depression of high-concentration pyrite in copper flotation by high pH. *Miner. Eng.* **2024**, *209*, No. 108651.

(10) Huang, L. H.; Chen, Y. M.; HuangW, W.; Wu, C. N.; Weng, L.; Liu, K. Experimental study on defoaming of flotation concentrate with different defoamers and their effect on flotation. *Conserv. Util. Miner. Resour.* **2022**, *42* (01), 106−111.

(11) Bhakta, A.; Ruckenstein, E. Drainage and Coalescence in Standing Foams. *J. Colloid Interface Sci.* **1997**, *191* (1), 184−201.

(12) Wu, L.; W, X.G.X. Experimental Study on Physical Defoaming of Anthracite Flotation Concentrate. *Coal Eng.* **2015**, *47* (01), 118−123.

(13) Liqin, R. E. N.; G, J. D. G. Study on vacuum defoaming test of flotation foam in laboratory. *Coal Sci. Technol.* **2018**, *46* (S1), 252−255.

(14) Takesono, S.; et al. Performance characteristics of mechanical foam-breakers fitted to a stirred-tank reactor. *J. Chem. Technol. Biotechnol.* **2003**, *78* (1), 48−55.

(15) Goldberg, M.; Rubin, E. Mechanical Foam Breaking. *Industrial & Engineering Chemistry Process Design and Development* **1967**, *6* (2), 195−200.

(16) Wang, P.; et al. Novel mechanical foam breaker based on self-oscillation for promoting the application of foam drilling technology. *Chem. Eng. Sci.* **2018**, *188*, 121−131.

(17) Liu, Y.; et al. Enhancing defoaming using the foam breaker with perforated plates for promoting the application of foam fractionation. *Sep. Purif. Technol.* **2013**, *120*, 12−19.

(18) Garrett, P. R. Defoaming: Antifoams and mechanical methods. *Curr. Opin. Colloid Interface Sci.* **2015**, *20* (2), 81−91.

(19) Yuan, J. Analysis on the Defoaming Mechanism of Defoamer. *OAJRC Material Science* **2023**, *4* (1), 22−25.

(20) Chou, Y.; Wu, F.; Shih, W. Toward numerical modeling of fine particle suspension using a two-way coupled Euler−Euler model: Part 2: Simulation of particle-induced Rayleigh−Taylor instability. *International Journal of Multiphase Flow* **2014**, *64*, 44−54.

(21) Chou, Y.; Wu, F.; Shih, W. Toward numerical modeling of fine particle suspension using a two-way coupled Euler−Euler model. Part 1: Theoretical formulation and implications. *International Journal of Multiphase Flow* **2014**, *64*, 35−43.

(22) Massoth, F. E. Oxidation of Coked Silica-Alumina Catalyst. *Industrial & Engineering Chemistry Process Design and Development* **1967**, *6* (2), 200−207.

(23) Ramadan, A.; Kuru, E.; Saasen, A. Critical review of drilling foam rheology. *Annu. Trans. - Nord. Rheol. Soc.* **2003**, *11*, 63−72.

(24) Ahmed, R. M.; et al. Rheology of foamed cement. *Cem. Concr. Res.* **2009**, *39* (4), 353−361.

(25) Llewellin, E. W.; Manga, M. Bubble suspension rheology and implications for conduit flow. *Journal of Volcanology and Geothermal Research* **2005**, *143* (1), 205−217.

(26) Luo, J. Y.; Gosman, D. Prediction of Impeller Induced Flows in Mixing Vessels using Multiple Frames of Reference. In *4th European Conf. on Mixing*, Institute of Chemical Engineers Symposium Series, 1994.

(27) Mansheng, S. Numerical Analysis of a Tailings Dam Break Based on FLUENT. *Copper Eng.* **2019**, *04*, 56−59.

(28) Pengwen, G. A. O.; W, G. Flow Field Distribution in Flash Copper Waste Heat Boiler Based on CFD. *Copper Eng.* **2023**, *03*, 159−165.

(29) Lane, G. L.; Schwarz, M. P.; Evans, G. M. Chapter 34 - Comparison of CFD Methods for Modelling of Stirred Tanks. In *10th European Conference on Mixing*; van den Akker, H. E. A.; Derksen, J. J.; Elsevier Science: Amsterdam, 2000, 273−280.

(30) Jahoda, M.; et al. CFD Modelling of Liquid Homogenization in Stirred Tanks with One and Two Impellers Using Large Eddy Simulation. *Chem. Eng. Res. Des.* **2007**, *85* (5), 616−625.

(31) Jaworski, Z.; et al. CFD Study of Homogenization with Dual Rushton Turbines—Comparison with Experimental Results: Part I: Initial Studies. *Chem. Eng. Res. Des.* **2000**, *78* (3), 327−333.

(32) Shuai, L.; et al. Simulation of the solid particles behavior in 3D stirred tank using CFD-DEM coupling approach. *Particulate Science and Technology* **2022**, *40* (8), 911−921.

(33) Li, S.; et al. CFD−PBM Simulation on Bubble Size Distribution in a Gas−Liquid−Solid Flow Three-Phase Flow Stirred Tank. *ACS Omega* **2022**, *7* (2), 1934−1942.

https://doi.org/10.1021/acsomega.4c04351
ACS Omega 2024, 9, 42850−42857